45th AIAA Aerospace Sciences Meeting & Exhibit, January 8-11, 2007, Reno, NV

Two- and Three-Dimensional Iced Airfoil Separation Bubble Measurements by Particle Image Velocimetry

Jason J. Jacobs* and Michael B. Bragg†

University of Illinois at Urbana-Champaign, Urbana, IL, 61801, USA

The separation bubble on a NACA 0012 airfoil with two- and three-dimensional, simulated, leading-edge, glaze-ice accretions was investigated using Particle Image Velocimetry (PIV). Chordwise PIV measurements, or those along the separation bubble cross-section, were obtained at a Reynolds number of 0.9x10^6, Mach number of 0.20, and between 0-deg and 5-deg angle-of-attack. Surface oil-flow visualization indicated increasing separation bubble length with airfoil angle-of-attack. Shorter separation bubble length at constant angle-of-attack and spanwise flow inside the separation bubble were also observed behind the three-dimensional ice simulation. Time-averaged PIV results revealed a primary recirculation with clockwise rotation defined by a shear layer and a smaller, secondary recirculation with counter-clockwise rotation directly downstream of the point of separation, both consistent with backward-facing-step-type flowfields. Mean and RMS velocity component contours highlighted these features and surface-normal profiles were extracted and compared to identify similarities and differences between the ice accretion flowfields which might explain the varying separation bubble lengths and spanwise instability observed in the flow visualization.

I. Introduction

Ice accretion on an airfoil surface changes the shape and thus the flowfield, pressure distribution, and aerodynamic performance of the airfoil. In general this means increased drag, reduced maximum lift and premature stall, variation in pitching moment, and overall reduction in control surface effectiveness. Due to these undesirable effects and their implications for flight safety, understanding the ice accretion process and the aerodynamic performance of iced airfoils is very important. The following describes this flowfield in detail and briefly summarizes select studies conducted to investigate it.

In many cases, ice accretion takes place on the airfoil leading-edge creating a formation centered at the stagnation point with backward-facing-step-like geometries on both the pressure and suction surfaces. Bragg et al.[1] provides a description of the flowfield resulting from this type of leading-edge modification, a schematic of which is presented in Fig. 1. As Bragg describes, the laminar or transitional boundary layer separates off the suction surface horn due to a sufficiently strong adverse pressure gradient and a shear layer forms between this separated region and the inviscid flow above. Pressure recovery is delayed in this region resulting in a constant pressure plateau until the shear layer transitions to turbulent flow. Vortex motion within the shear layer entrains higher velocity inviscid flow and mixes it with lower velocity flow in the separated region. At sufficiently low angle-of-attack, this mixing promotes pressure recovery and the flow reattaches as a turbulent boundary layer. This reattachment is unsteady and defines a separation bubble whose size and shape vary

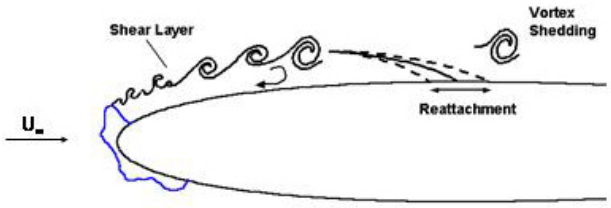

Fig. 1. Schematic of Separation Bubble on Airfoil With Leading-Edge Ice Accretion[2]

*Graduate Research Assistant, Department of Aerospace Engineering, Member AIAA.

†Professor, Department of Aerospace Engineering, Associate Dean for Research and Administrative Affairs, Fellow AIAA.

in time. At larger angles-of-attack where the required pressure recovery cannot be achieved, reattachment occurs intermittently or not at all. This results in a bubble bursting phenomenon which initiates premature airfoil stall.

Gurbacki and Bragg[2] and Gurbacki[3] conducted time-averaged and unsteady surface-pressure measurements, wake surveys, surface oil-flow visualization, and Particle Image Velocimetry (PIV) on a NACA 0012 airfoil with two- and three-dimensional, simulated, leading-edge, glaze-ice accretions. In these studies, the cross-section of the two-dimensional ice simulation was representative of the average cross-section of the three-dimensional ice simulation. For both of the simulated accretions, the mean reattachment length, as well as the chordwise extent of the reattachment zone (unsteady bubble length variation), were shown to increase with angle-of-attack up to stall which was reduced approximately 10-deg by the accretions. Power spectra of time-dependent surface-pressure data near reattachment also revealed unsteadiness with nondimensional frequency $S_t = fx_{MR}/V_\infty = 0.53 - 0.73$ attributed to shear-layer vortices and vortex shedding from the separation bubble. Here f is the dimensional frequency, x_{MR} is the location of mean reattachment or bubble length, and V_∞ is the freestream velocity. Furthermore, broadband low-frequency unsteadiness was reported near stall with $S_t = 0.01$ based on time-dependent surface-pressure integrated lift coefficient power spectra. Because of its frequency, this unsteadiness was thought to be a vertical oscillation or flapping of the shear layer. Both unsteady modes are consistent with separation bubble unsteadiness reported in backward-facing step flows by Eaton and Johnston[4] and Driver et al.[5] and in blunt flat plate flows by Kiya and Sasaki[6,7] and Cherry et al.[8]

Gurbacki and Bragg[2] and Gurbacki[3] further compared the time-averaged and unsteady flowfields and performance of the constant span, two-dimensional, ice simulation with that of the three-dimensional, cast ice simulation. The most striking difference between the two was revealed in the surface oil-flow visualization which showed a significant reduction in bubble length behind the three-dimensional ice simulation. Furthermore, this separation bubble was non-uniform in the spanwise direction, consisting of cells that did not correspond to noticeable features along the span of the three-dimensional ice simulation. These cells were attributed to a spanwise instability excited by the casting roughness which produced streamwise vortex structures that curved the streamlines within the separation bubble, particularly near the separation and reattachment lines. It was also proposed that these structures enhanced mixing between the inviscid flow and separation bubble, aiding pressure recovery, shortening bubble length, and reducing the maximum lift coefficient and stall angle penalty relative to the two-dimensional ice simulation. A similar spanwise instability was observed in linear stability analyses of DNS of backward-facing step flow by Barkley[9] and laminar separation bubble flow by Theofilis.[10,11]

As demonstrated by this brief review, much research has focused on separation bubbles from geometries such as the backward-facing step and blunt flat plate as well as clean airfoils and those with leading-edge ice accretions. Despite this attention, however, few detailed quantitative flowfield measurements have been taken to characterize the separation bubble, particularly related to the vortical flow structure which is closely related to shear-layer reattachment and boundary-layer development downstream. Therefore the objective of this investigation is to improve the understanding of iced airfoil separation bubble and other unsteady, largely separated, reattaching flowfields and provide data useful in improving the computational methods used to predict them.

II. Experimental Methods

Experiments were performed at the University of Illinois Aerodynamics Research Laboratory (ARL) in a 15x15-inch test section, subsonic wind tunnel. The 48-inch long test section was preceded by a 29:1 area ratio inlet contraction section and an inlet settling section containing a 4-inch thick expanded aluminum honeycomb flow straightener and four 24-mesh, stainless steel, turbulence-reducing screens. Downstream of the test section was a 4-deg equivalent cone angle diffuser connecting a 125-Hp, 16-bladed, axial fan. This facility was constructed specifically for this PIV investigation, therefore, the test section incorporated a glass sidewall and ceiling panel for laser and camera optical access and the fan could be exhausted into the tunnel room or outdoors through a 90-deg turning vane exhaust section, as was done when the flow was seeded for PIV.

The airfoil model used for this investigation was an 8-inch chord, 14.95-inch span, solid aluminum, NACA 0012. Surface static pressure and PIV data were acquired on the clean model for validation purposes, however, the geometries of greatest interest were the airfoil model with two- and three-dimensional, simulated, leading-

edge, glaze-ice accretions. The two-dimensional ice simulation was a geometrically-scaled model of that tested by Gurbacki and Bragg[2] and Gurbacki[3] in the ARL 3x4-foot wind tunnel and is shown in Fig. 2. The original accretion was acquired by Gurbacki on an 18-inch chord, 22-inch span NACA 0012 model at 4-deg angle-of-attack in the BF-Goodrich Icing Wind Tunnel. A mold was taken of this accretion from which the three-dimensional ice simulation casting was produced using a polyurethane elastomer technique developed at the NASA Glenn Research Center.[12] An additional casting was produced, cut, and traced allowing a representative cross-section to be defined which was extruded and manufactured using stereolithography to produce the original two-dimensional ice simulation. This is the same geometry which has been scaled and manufactured, also using stereolithography, for PIV testing. Because the original three-dimensional ice simulation casting could not be geometrically-scaled, 20-grit roughness elements were adhered to a duplicate two-dimensional ice simulation using epoxy resin to create the three-dimensional ice simulation used for PIV testing shown in Fig. 2. This simulation technique was shown to most closely reproduce the flowfield behind the three-dimensional ice simulation casting in a series of surface oil-flow visualization experiments on both the 18-inch and 8-inch chord models. Finally, both the airfoil model (visible in Fig. 3) and the two- and three-dimensional ice simulations (Fig. 2) were coated with a Rhodamine-6G based fluorescent paint which combined with a 532±10-nm (green) band-pass filter attached to the PIV camera lens, significantly reduced laser reflections which would have otherwise contaminated vector correlations near the model surface.

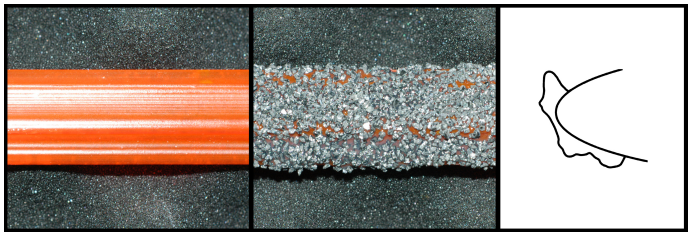

Fig. 2. Two- and Three-Dimensional Ice Simulations and Cross-Section Tested Using PIV

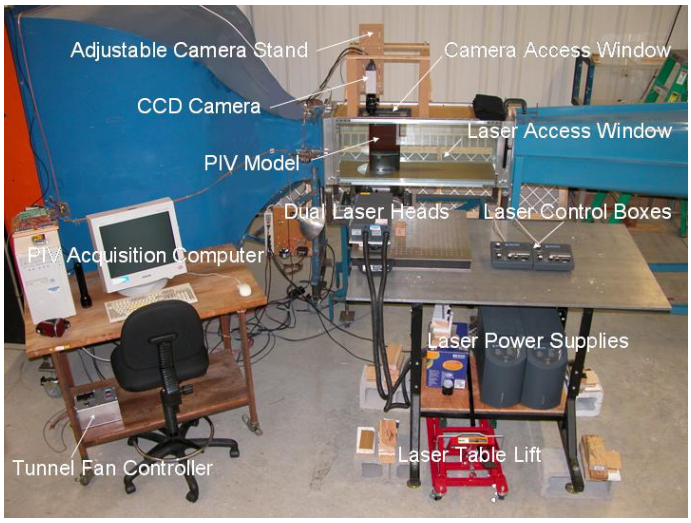

Fig. 3. LaVision FlowMaster 3S PIV System Setup

All experiments were performed at a Reynolds number of 0.9×10^6 and Mach number of 0.20. Prior to acquiring PIV data, steady pressure distributions were acquired using a Pressure Systems Incorporated 8400 electronic scanning pressure (ESP) system between -5-deg and 6-deg angle-of-attack in one degree increments, the upper limit imposed to prevent saturation of the 1-psi ESP transducer module. All model pressure taps and those located in the settling section and test section inlet from which test section dynamic pressure and freestream velocity were derived, were sampled at 100-Hz for one second and time averaged. Surface oil-flow visualization was also performed on the model with each ice simulation prior to acquiring PIV data in order to map the separation bubble length and reattachment zone versus angle-of-attack and to locate spanwise cell structures behind the three-dimensional ice simulation for future spanwise PIV measurements. A mineral oil and fluorescent dye mixture was sprayed on the model and the tunnel run for approximately 60 seconds during which time the mixture would flow over the model surface, driven by the local shear. The results were illuminated with ultra-violet lighting and photographed for later processing using a Nikon D100 digital SLR camera with a 35-105-mm Nikkor zoom lens with haze filter. This process was performed between 0-deg and 6-deg angle-of-attack in one degree increments.

PIV measurements were then acquired using the LaVision FlowMaster 3S PIV system shown in Fig. 3 which consisted of a dual 120-mJ Gemini Nd:YAG PIV laser, a Kodak ES1.0 1-megapixel cross-correlation PIV camera, and a dual 600-MHz processor acquisition computer running Microsoft Windows XP and LaVision's Data Acquisition and Visualization Software (DaVis) v6.2. Flow seeding was provided by two TSI Model 9307 Laskin nozzle type oil droplet generators, producing 1.0-μm mean diameter particles, and two TSI Model 9306 six-jet atomizers, producing 0.6-μm mean diameter particles, each filled with olive

oil. The seeding particles were introduced in front of the inlet settling section using a 4-inch diameter PVC manifold with two rows of six 1/2-inch nozzles which was positioned and oriented to uniformly seed the area of interest. This area was illuminated by a laser sheet which entered the test section through the glass sidewall, oriented parallel to the tunnel floor, at a spanwise location determined by the height of the laser table. The camera imaged this area from above through a glass panel installed in the test section ceiling. Measurements were acquired between 0-deg and 5-deg angle-of-attack in one degree increments, the range over which separation bubble reattachment occurred on the suction surface according to surface oil-flow visualization. One thousand image pairs were acquired at each angle-of-attack at a constant rate of approximately 3 pairs per second, limited by the frame rate of the camera in cross-correlation mode and the speed and memory of the acquisition computer. A 60-mm Nikkor lens delivered a field-of-view of approximately 1.6-inches, or 19% chord. The correlation analysis, performed on a 2.6-GHz Microsoft Windows XP machine using LaVision's DaVis v6.2, was a multi-pass adaptive algorithm with an interrogation cell size of 32 pixels square yielding a vector spacing of approximately 0.025-inches at 50% overlap. Vector validation was by a median filter routine which identified spurious vectors based on spatial RMS variation and replaced them with the average of neighboring vectors. All other processing was performed in MATLAB v6.1 using subroutines developed at Illinois.

III. Results and Discussion

A. Steady Pressure Distributions

Clean model, steady pressure distributions and those with the two- and three-dimensional ice simulations were acquired and compared to data by Gurbacki. These measurements, which were reported by Jacobs and Bragg[13] and are summarized below, were taken to verify that the flowfields generated on the 8-inch chord model for PIV investigation were consistent with those examined by Gurbacki and Bragg[2] and Gurbacki[3] on the 18-inch chord model in the ARL 3x4-foot wind tunnel.

The steady pressure distributions on the clean 8-inch chord PIV model were virtually identical to those on the clean 18-inch chord model. With the two-dimensional ice simulation, however, a somewhat shorter separation bubble was observed on the PIV model, thought to be the result of manufacturing tolerances and positioning errors of the two-dimensional ice simulation on that model. Likewise with the 20-grit, three-dimensional ice simulation, the PIV model steady pressure distributions varied somewhat from those on the 18-inch chord model with the three-dimensional ice casting, however, closely matched data from a 14-grit, three-dimensional ice simulation on the same 18-inch chord model by Busch.[14]

These results indicated that the clean and iced pressure distributions on the PIV model were similar to those on the 18-inch chord model. In addition, surface oil-flow visualization reported by Jacobs and Bragg[13] showed very similar behavior in separation bubble length versus angle-of-attack and in the spanwise cell spacing behind the three-dimensional ice casting and simulation. Based on these results and the objective of this investigation, namely to characterize and understand the flowfields around an airfoil with simulated, two- and three-dimensional, leading-edge glaze-ice accretions similar to those examined by Gurbacki and Bragg[2] and Gurbacki[3] on the 18-inch chord model, the flowfields generated on the 8-inch chord model were deemed appropriate.

B. Surface Oil-Flow Visualization

Flow visualization was performed on the PIV model to document separation bubble length versus angle-of-attack as well as spanwise cell spacing behind the three-dimensional ice simulation for future spanwise PIV measurements. Figure 4 shows two of these images at 4-deg angle-of-attack, with the two-dimensional ice simulation presented in Fig. 4(a) and the three-dimensional ice simulation in Fig. 4(b). In both cases, flow is from left to right and the ice simulation is visible on the left side of the image. Finally, the tape applied along the chord and span in each image indicates percent chord, x/c, from 0% to 100% and spanwise location, z, in 1/2-inch increments, respectively. Both scales are used to locate important flow features such as mean reattachment and spanwise cell structures within an uncertainty of approximately $\pm 1.4\%$ chord and $\pm 0.8\%$ span, respectively, based on the uncertainty of marking and applying the reference tape, locating these flow features in an image, and interpolating their position.

As discussed in Section I and illustrated in Fig. 1, the flow separates from the horn on the upper surface of the ice shape generating a shear layer separating a low velocity, recirculating separation bubble from

the inviscid flow above. Vortices in the shear layer entrain higher energy flow into the separation bubble initiating pressure recovery at sufficiently low angle-of-attack. This results in flow reattachment farther downstream, an unsteady process which in the mean appears as a thin, speckled region as seen near 34% chord in Fig. 4(a); the center of this region is considered mean reattachment. Upstream of this location inside the separation bubble, the flow is low velocity and clockwise recirculating, and downstream the flow has reattached as a turbulent boundary layer. Also referring to Fig. 4, note the spanwise variation within each separation bubble. Behind the two- dimensional ice simulation, the mean reattachment line is straight and the streamlines inside the separation bubble are parallel to the freestream. Behind the three-dimensional ice simulation, however, the streamlines inside the separation bubble are curved indicating the presence of a spanwise velocity component, w. This is the instability discussed in previous sections whose origin will be investigated in detail through future spanwise PIV measurements.

Figure 5 summarizes the location of mean reattachment versus angle-of-attack of the original ice simulations presented by Jacobs and Bragg[13] and the new (current) ice simulations with error bars indicating a ±1.4% chord uncertainty in these estimates. The original ice simulation mean reattachment data were spanwise averaged between 20% and 80% span, the portion of the model not influenced by the tunnel walls at the angles-of-attack of interest. The current two- and three-dimensional ice simulation mean reattachment data, however, were averaged at 47% and 64% span and between 47% and 54% span in 1.7% span increments, respectively, the same spanwise locations where PIV measurements were acquired on each corresponding simulation. This had little effect on the estimate of mean reattachment of the original two- and three-dimensional and the current two-dimensional ice simulations as these mean reattachment zones were not strong functions of span. As shown in Fig. 4(b), however, the mean separation bubble behind the current three-dimensional ice simulation was slightly enlarged toward the top of the model due to a build-up of epoxy used to adhere the roughness elements to the ice simulation. Averaging mean reattachment only where PIV data were acquired, therefore, allowed a more direct comparison.

Again referring to Fig. 5, the current ice simulations produced separation bubbles up to 10% chord longer than the original ice simulations, most likely due to small variations in the alignment and orientation of the ice simulation on the airfoil model. In

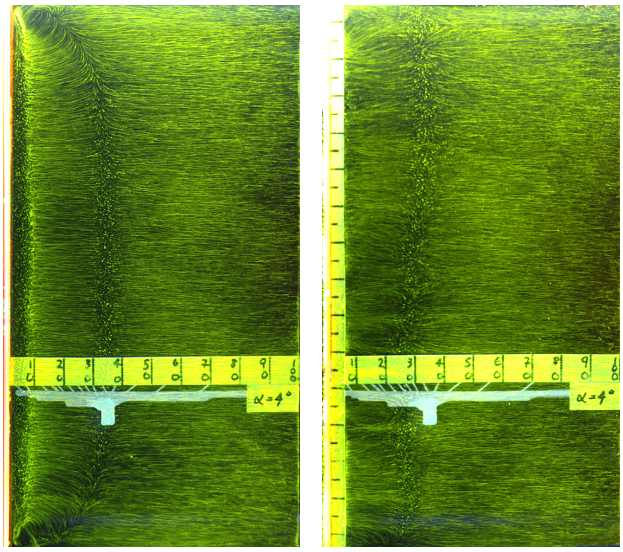

(a) 2D (b) 3D

Fig. 4. Surface Oil-Flow Visualization With 2D and 3D Ice Simulations (Flow Left to Right, R_e=0.9x10^6, M_∞=0.20, α=4-deg)

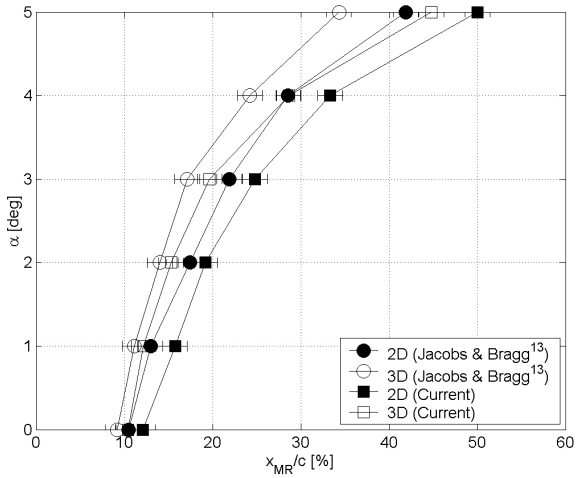

Fig. 5. Mean Reattachment From Surface Oil-Flow Visualization (R_e=0.9x10^6, M_∞=0.20)

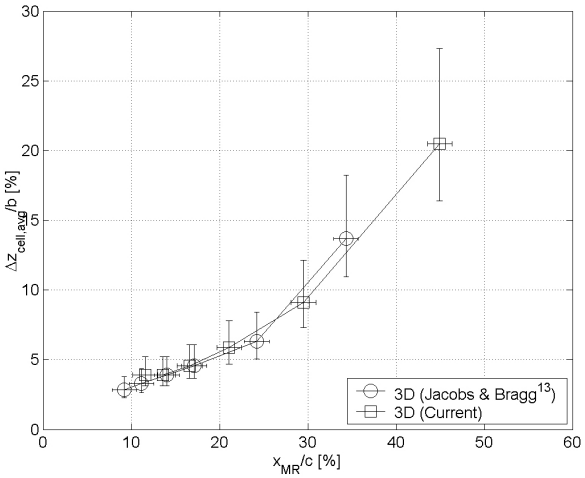

Fig. 6. Average Spanwise Cell Spacing Behind 3D Ice Simulations From Surface Oil-Flow Visualization (R_e=0.9x10^6, M_∞=0.20)

both cases, however, the shear layer reattaches farther upstream behind the three-dimensional ice simulation than the two-dimensional. Gurbacki[3] suggests this is due to the same vortex structures which generate three-dimensional flow inside the separation bubble behind the three-dimensional ice simulation. These vortices potentially aid in the entrainment of higher energy flow into the separation bubble, further promoting pressure recovery and shortening bubble length. While this has been reported in the literature, such as by Westphal and Johnston[15] who noted shortened reattachment lengths downstream of a backward-facing step when small triangular vortex generators were placed upstream of the separation point, a thorough PIV investigation of these vortex structures, including their relationship to separation bubble length, is currently underway.

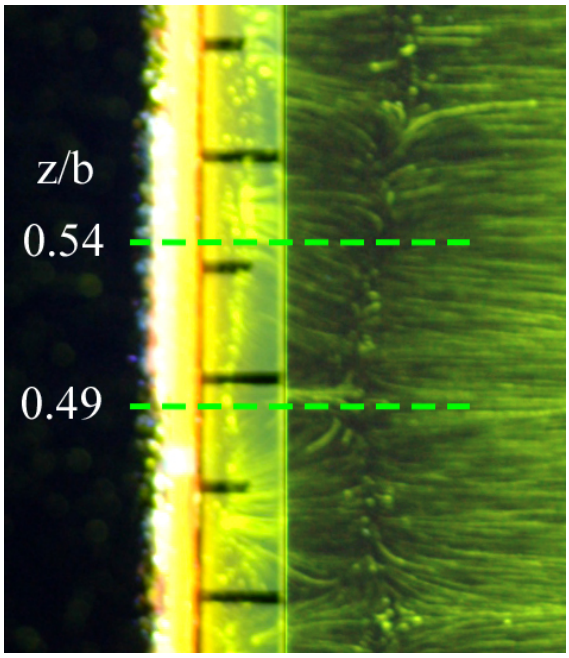

Fig. 7. Spanwise Locations of Select PIV Measurements of the 3D Ice Simulation (Flow Left to Right, R_e=0.9x10^6, M_∞=0.20, α=0-deg, x_{MR}/c=9.4%)

While the original and current ice simulations produced varying separation bubble lengths, it was not expected that the fundamental structure of these flowfields, which was of primary interest to this PIV investigation, was any different. This was supported by examining the average spanwise cell spacing behind the two three-dimensional ice simulations. It has been observed that this spacing was related to separation bubble length and the flow visualization results obtained here were consistent with this hypothesis. At smaller angles-of-attack, the shorter separation bubbles consisted of a larger number of more closely spaced spanwise cells than did the longer separation bubbles at larger angles-of-attack. This notion can also be found in the literature, such as in a study by Barkley[9] who performed linear stability analyses on backward-facing step DNS and found the critical eigenmode to be a spanwise periodic structure similar to the spanwise cells observed in Fig. 4(b). By studying the instability mechanism, he argued the instability was centrifugal in nature according to Rayleigh's criterion[16] in which recirculating flow, such as that inside the separation bubble, can give rise to out-of-plane secondary flow depending on the distribution of angular momentum. Because it was the eddies inside this recirculating region which drove the instability, it was the length of this region which was the appropriate length scale for the instability. This is supported in Fig. 6 where the average spanwise cell spacing behind the three-dimensional ice simulations in percent span, estimated by dividing the model span by the total number of spanwise cells observed in flow visualization images, is plotted versus separation bubble length in percent chord. Because these cell structures can be difficult to distinguish, their average spacing could not be determined within the same uncertainty as the location of mean reattachment as indicated by the vertical error bars in Fig. 6. These uncertainties represent a $\pm$25% variation in the total number of observed spanwise cells, however, these relationships do show spanwise cells growing larger and fewer in number with increasing separation bubble length. Furthermore, the original and current three-dimensional ice simulation flowfields compare well when the separation bubble length and spanwise cell spacing are normalized in this manner as did the original three-dimensional ice simulation and casting flowfields as demonstrated by Jacobs and Bragg.[13]

The final surface oil-flow visualization results presented are found in Fig. 7, where the spanwise location of two chordwise PIV measurements of the three-dimensional ice simulation presented in the next section are illustrated relative to surrounding spanwise cell structures. Note at zero angle-of-attack, the PIV measurements at 49% span correspond to the intersection of two cell structures, a concave cell from above and a convex cell from below. Their interaction produces a diamond-shaped pattern across the reattachment zone with maximum spanwise velocity centered at mean reattachment. The PIV measurements at 54% span, however, are located toward the center of a single spanwise cell as the surface streamlines above and below are parallel (although not with the freestream) and the reattachment zone is quasi-two-dimensional.

C. Particle Image Velocimetry

This investigation involves PIV measurements along multiple chordwise and spanwise planes of the 8-inch chord PIV model with both the two- and three-dimensional ice simulations. Jacobs and Bragg[13] presented chordwise PIV measurements of the original two-dimensional ice simulation and this paper will compare chordwise PIV measurements of the current two- and three-dimensional ice simulations. Finally, spanwise PIV measurements may be found in the dissertation detailing this investigation which is currently underway and in future publications.

Figure 8 shows instantaneous images of the seeded flow over the two- and three-dimensional ice simulations at select spanwise stations, all at zero degrees angle-of-attack. The model is visible at the bottom of each image and the ice simulation, at the bottom left. Laser reflections off the model and ice simulations were minimal due to the fluorescent paint and PIV camera lens filter combination, however, the roughness applied to the three-dimensional ice simulation was not painted, hence the brighter reflection off the horn of this simulation. Also note the separation bubble extending from the back of each ice simulation to mean reattachment near 12%, 8%, and 11% chord, respectively, and the shear layer emanating from the tip of each ice simulation horn, separating the bubble from the inviscid flow above. In the case of the two-dimensional ice simulation, the top of this shear layer follows the curvature of the airfoil until near mean reattachment. The shear layer extending from the horn of the three-dimensional ice simulation, however, appears less convex at z/b=0.49, near the intersection of two spanwise cells as described previously, but resumes a curved trajectory at z/b=0.54, toward the center of another spanwise cell. This distinction will be more apparent in flowfield properties presented later. In addition, vortices are seen inside each shear layer as small regions of low seed concentration where the flow rotation has centrifuged the higher-than-air-density olive oil particles away from the vortex core. Vortices are also visible downstream of mean reattachment supporting previous findings of separation bubble vortex shedding such as by Kiya and Sasaki.[6]

A correlation analysis was performed on each PIV image pair using LaVision's DaVis v6.2 resulting in a single instantaneous velocity vector field. After all image pairs were correlated and validated using a LaVision spatial RMS median filter algorithm, further calculations proceeded in MATLAB v6.1. These included further validation by a corresponding temporal RMS median filter and near surface velocity filter algorithms and the calculation of

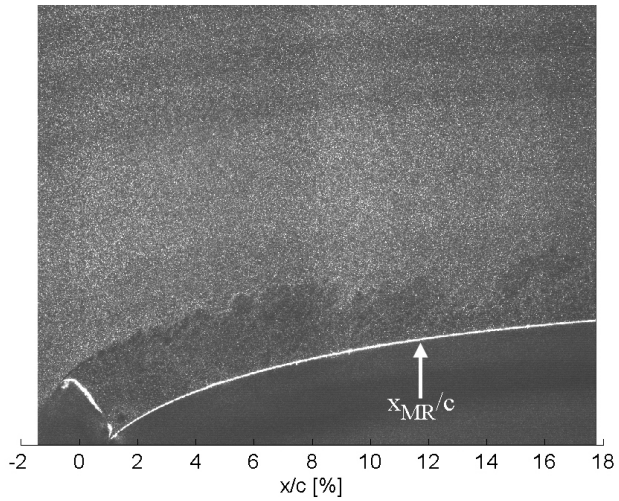

(a) 2D Ice Simulation (z/b=0.47)

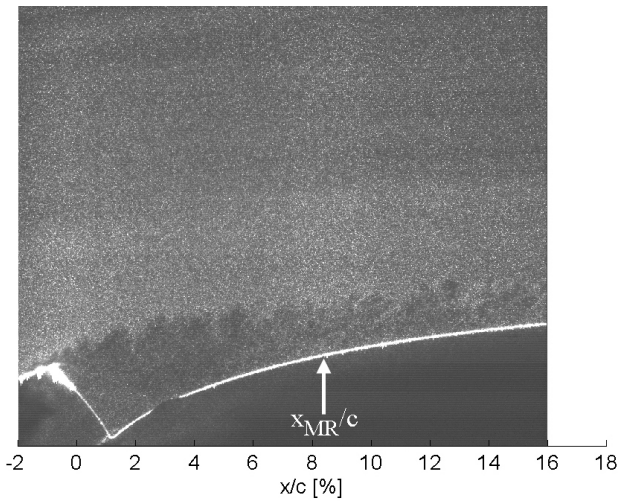

(b) 3D Ice Simulation (z/b=0.49)

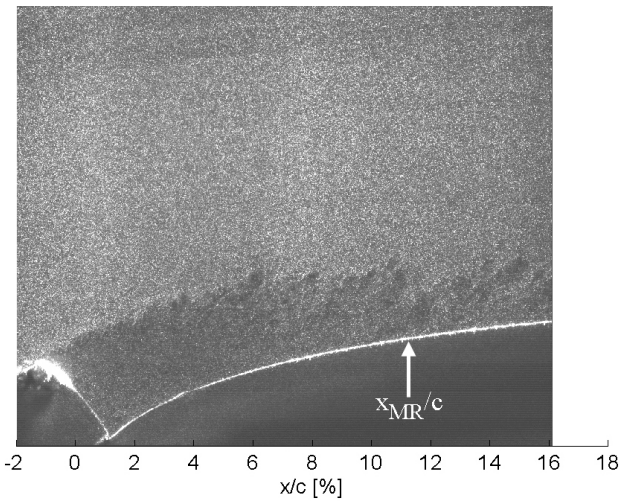

(c) 3D Ice Simulation (z/b=0.54)

Fig. 8. Instantaneous Seeded Flow Images of PIV Model With Ice Simulation (Flow Left to Right, R_e=0.9x10^6, M_∞=0.20, α=0-deg, Freestream Cropped)

various time-averaged and fluctuating flowfield properties and statistics. Mean reattachment was also estimated from PIV measurements based on the chordwise distribution of forward flow intermittency and skin friction as described by Jacobs and Bragg.[13] Figure 9 summarizes these mean reattachment calculations versus angle-of-attack for both ice simulations and compares them to surface oil-flow visualization results. In all cases except the three-dimensional ice simulation at 5-deg angle-of-attack, PIV yielded a smaller separation bubble than flow visualization. Excluding the three-dimensional ice simulation at 3-deg and 4-deg angles-of-attack, however, this difference was within the uncertainty of the flow visualization estimate, consistent with the agreement obtained on the original two-dimensional ice simulation by Jacobs and Bragg.[13] The source of the disagreement at 3-deg and 4-deg angles-of-attack with the three-dimensional ice simulation is not currently known.

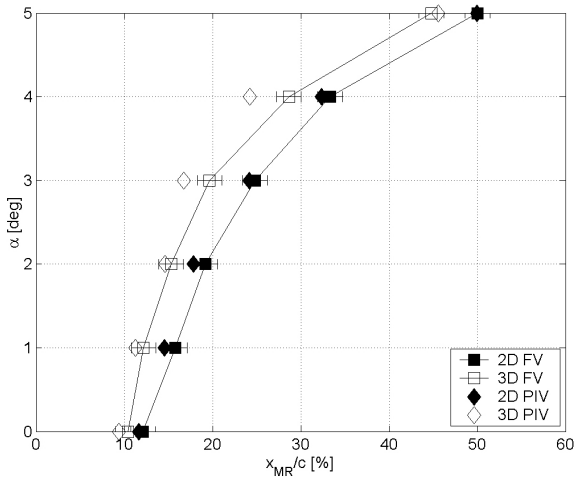

Fig. 9. Comparison of Mean Reattachment of Current Ice Simulations From Surface Oil-Flow Visualization and PIV (R_e=0.9x10^6, M_∞=0.20)

Streamlines integrated from the time-averaged velocity vector fields and forward flow intermittency, the percentage of vector realizations with positive streamwise velocity, are presented in Figs. 10-15 for each configuration illustrated in Fig. 8. Superimposed onto each streamline figure are two additional streamlines as defined by Khodadoust[17] which are representative of the time-averaged separation bubble. The lower, or stagnation streamline, indicates the height above the wall where the time-averaged streamwise velocity component, $\overline{u}$, is zero, and divides the reverse flow in the lower half of the separated region from the forward flow above. The upper, or separation streamline, indicates the height above the wall, y_{sep}, below which the streamwise mass-flow per unit span is zero in a time-averaged sense and for a uniform density flow is given by:

$$\int_{y_{surf}/c}^{y_{sep}/c} \frac{\overline{u}}{V_\infty}\, d\left(\frac{y}{c}\right) = 0\,. \tag{1}$$

This streamline perhaps better illustrates the time-averaged separation bubble as it extends above the stagnation streamline until there is zero net streamwise mass-flow below, as if the mean separation bubble was replaced by a solid wall. A third streamline representing the time-averaged separation bubble is superimposed onto each forward flow intermittency figure and indicates the height above the wall where this statistic reaches 50%, meaning half of the vector realizations along this streamline have positive streamwise velocity. This is the threshold used to locate mean reattachment from PIV measurements as described by Jacobs and Bragg,[13] therefore, the intersection of this streamline with the model surface indicates mean reattachment according to PIV.

Note in Figs. 10-12, the time-averaged flowfield consisted of a clockwise recirculating, primary separation region extending from behind the ice simulation to mean reattachment and a smaller, counter-clockwise recirculating, secondary separation region at the intersection of the ice simulation and airfoil model.[a] In each case, the stagnation streamline divides the concentric, elliptical flow streamlines of the primary recirculation region in half along the locus of points with zero mean streamwise velocity and just above, the separation streamline defines the outer edge of this region. Both the primary and secondary recirculation regions grow in length and height (parallel and perpendicular to the model chordline) with increasing angle-of-attack and both are characteristic of backward-facing-step-type flows such as those investigated by Kostas et al.[18] and Hudy et al.[19]

Comparing the stagnation and separation streamlines of the two-dimensional ice simulation in Fig. 10 with those of the three-dimensional ice simulation near the edge of adjacent spanwise cells (z/b=0.49) in Fig. 11, note how the former are convex, following the curvature of the airfoil as noted from the seeded flow images in Fig. 8, whereas the latter are flat and more aligned with the model chordline. This results in a smaller, more circular primary recirculation region behind the three-dimensional ice simulation at this spanwise location. This is also apparent from the corresponding concave 50% intermittency streamline presented in Fig. 14.

[a]The direction of recirculation is determined by the gradient of intermittency; an outwardly facing gradient indicates clockwise recirculation and vice-versa.

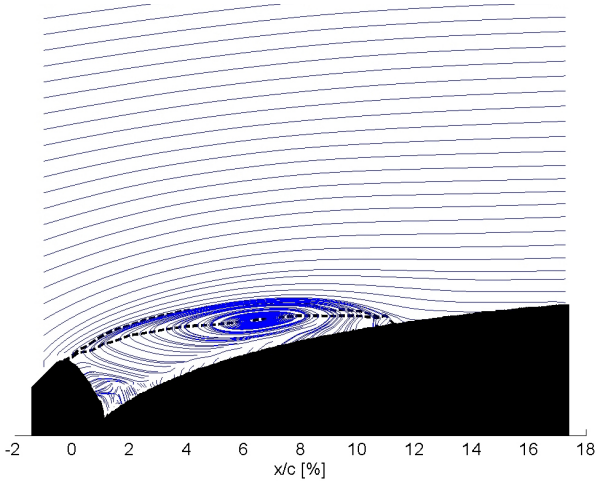

Fig. 10. Mean Streamlines [2D Ice Simulation (z/b=0.47), R_e=0.9x10^6, M_∞=0.20, α=0-deg, $--$ Sep.(Upper) and Stag.(Lower) Streamlines]

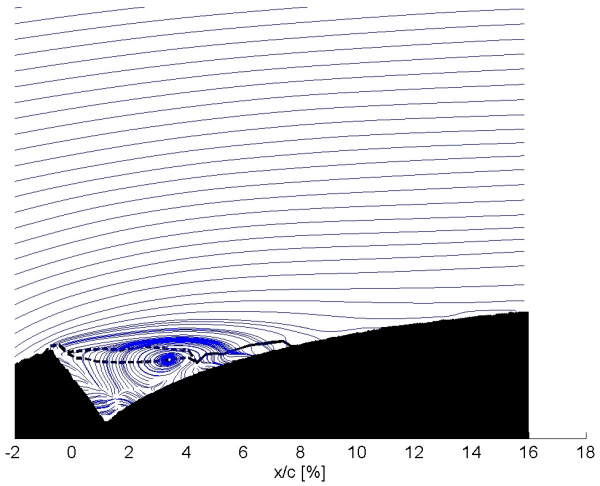

Fig. 11. Mean Streamlines [3D Ice Simulation (z/b=0.49), R_e=0.9x10^6, M_∞=0.20, α=0-deg, $--$ Sep.(Upper) and Stag.(Lower) Streamlines]

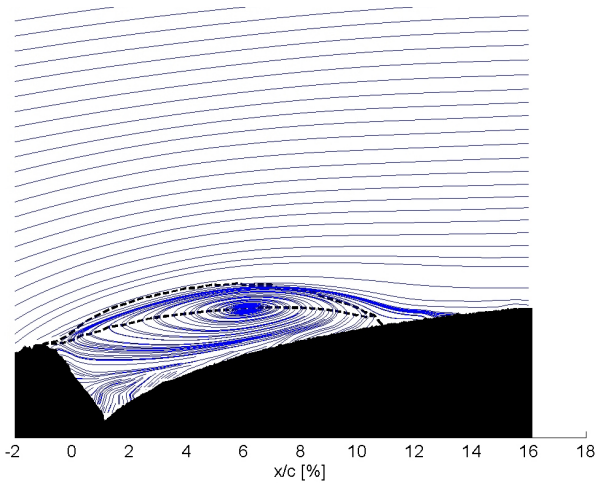

Fig. 12. Mean Streamlines [3D Ice Simulation (z/b=0.54), R_e=0.9x10^6, M_∞=0.20, α=0-deg, $--$ Sep.(Upper) and Stag.(Lower) Streamlines]

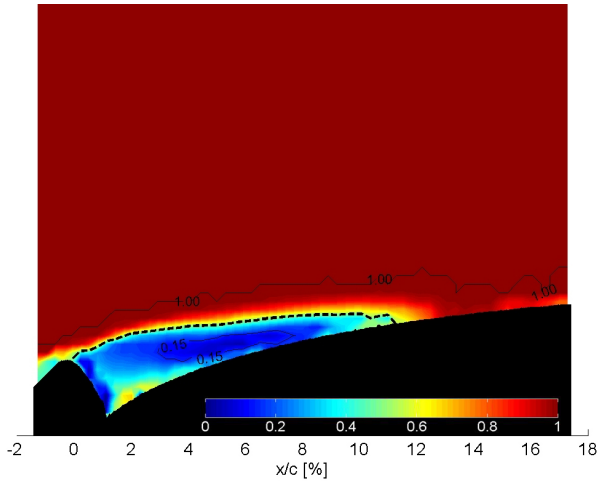

Fig. 13. Forward Flow Intermittency [2D Ice Simulation (z/b=0.47), R_e=0.9x10^6, M_∞=0.20, α=0-deg, x_{MR}/c=11.7%, $--$ 50% FFI Streamline]

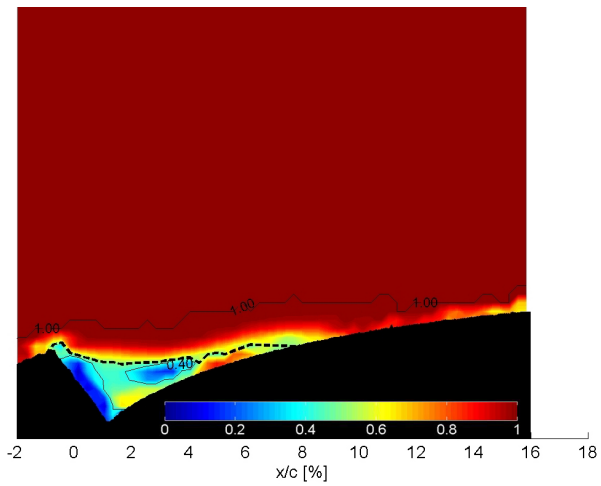

Fig. 14. Forward Flow Intermittency [3D Ice Simulation (z/b=0.49), R_e=0.9x10^6, M_∞=0.20, α=0-deg, x_{MR}/c=8.4%, $--$ 50% FFI Streamline]

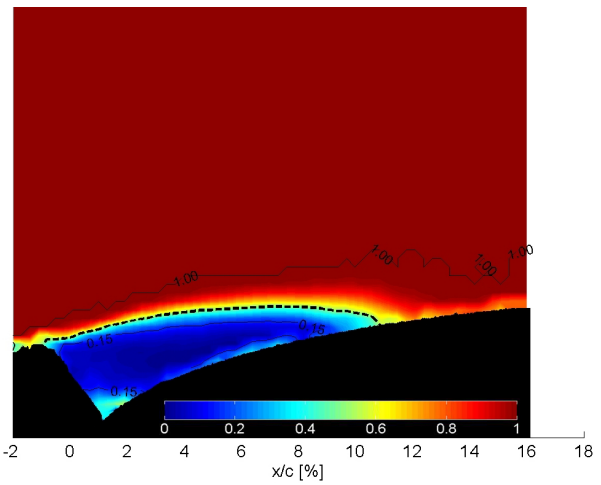

Fig. 15. Forward Flow Intermittency [3D Ice Simulation (z/b=0.54), R_e=0.9x10^6, M_∞=0.20, α=0-deg, x_{MR}/c=11.3%, $--$ 50% FFI Streamline]

Toward the center of a spanwise cell (z/b=0.54) where the surface streamlines are parallel, however, the flowfield behind the three-dimensional ice simulation in Fig. 12 is qualitatively very similar to that behind the two-dimensional ice simulation, but with a shorter (chordwise) and taller (normalwise) primary recirculation. This results in even more convex stagnation and separation streamlines with greater separation between them which translates to a thicker shear layer positioned farther from the surface of the model. This, again, is consistent with the more convex and taller (normalwise) region of low intermittency in Fig. 15. It should be noted at this point that these results represent two-dimensional slices of three-dimensional flowfields (more so with the three-dimensional ice simulation, of course) and must be interpreted accordingly, and that spanwise PIV measurements (those viewing a spanwise-normalwise plane) are currently being processed which will aid in this interpretation.

Mean and RMS streamwise velocity contours for the same configurations are presented in Figs. 16-21, all normalized by the freestream velocity. These results for the current two-dimensional ice simulation, presented in Figs. 16 and 19, are indistinguishable from those of the original two-dimensional ice simulation presented by Jacobs and Bragg.[13] The shear layer is visible in the mean streamwise velocity as the region across which this component accelerates from zero to the edge-velocity and in the RMS streamwise velocity as the region where large fluctuations are observed upstream of mean reattachment. From the point of flow separation until approximately 5% chord, this region is very thin, but then quickly expands toward the airfoil surface to near the height of the ice simulation normal to the airfoil surface. In addition, the separation streamline bisects this shear layer, connecting the locus of maximum RMS streamwise velocity, consistent with the identification of the shear-layer center by Kiya and Sasaki,[6] and along this streamline, two local maxima are observed. The larger, approximately 0.42, occurs just downstream of flow separation and the smaller, approximately 0.30, just upstream of mean reattachment before the RMS streamwise velocity decays as the shear layer reattaches as a turbulent boundary layer. The peak near mean reattachment is identical to that measured on the original two-dimensional ice simulation by Jacobs and Bragg[13] and close to the 0.34 measured by Khodadoust[17] on a NACA 0012 airfoil with a similar simulated, leading-edge, glaze-ice accretion at a Reynolds number of approximately 1.5×10^6 using laser Doppler velocimetry (LDV). Furthermore, this qualitative picture of the RMS streamwise velocity field is characteristic of backward-facing step type flows such as those examined by Kostas et al.[18] and Hudy et al.[19] and complements time-dependent surface pressure measurements by Gurbacki and Bragg[2] and Gurbacki[3] who noted peak RMS surface pressure just upstream of mean reattachment behind both the two- and three-dimensional ice simulations reproduced for this investigation. Finally, note the stairstep pattern near the airfoil surface in Fig. 19, the result of reduced effective interrogation cell size in this region. That is, as the airfoil surface is approached from the left along a line of constant y/c, more and more of each interrogation cell overlaps the image of the model (where the intensity is set to zero prior to the correlation analysis), reducing the effective interrogation cell size and increasing RMS velocity fluctuations. Fortunately, this region is very near the model surface (less than the 0.025-inch vector spacing) and does not significantly affect the separation bubble measurements.

Now, comparing this flowfield to that of the three-dimensional ice simulation near the edge of adjacent spanwise cells (z/b=0.49) in Figs. 17 and 20, the shear layer separating from the three-dimensional ice simulation appears thicker near the point of separation with higher intensity RMS streamwise velocity fluctuations, approximately 0.49. It also begins expanding toward the airfoil surface sooner, at approximately 3% chord, but reaches a maximum thickness closer to half of the ice simulation effective height. Finally, the local maximum RMS streamwise velocity upstream of mean reattachment is of lower intensity, approximately 0.25, and the separation streamline outlines the inner edge of the shear layer, not the center as in the case of the two-dimensional ice simulation. These differences, combined with the spanwise flow observed in the surface oil-flow visualization at this spanwise location, perhaps indicate a three-dimensional relieving effect, however, more analysis, including that of the spanwise PIV measurements, will be required to understand them.

And comparing the mean and RMS streamwise velocities around the two-dimensional ice simulation with those around the three-dimensional ice simulation at z/b=0.54 shows that, as with the time-averaged streamlines, the flowfields are qualitatively very similar. The important distinctions are that the shear layer is thicker and farther from the airfoil surface across the field-of-view, the RMS streamwise velocity fluctuations are of higher intensity, with local maxima approximately 0.45 and 0.32, and the separation streamline outlines the outer edge of the shear layer, not the center or the inner edge as behind the three-dimensional ice simulation at z/b=0.49.

RMS normal velocity contours are now presented in Figs. 22-24. The field around the current two-

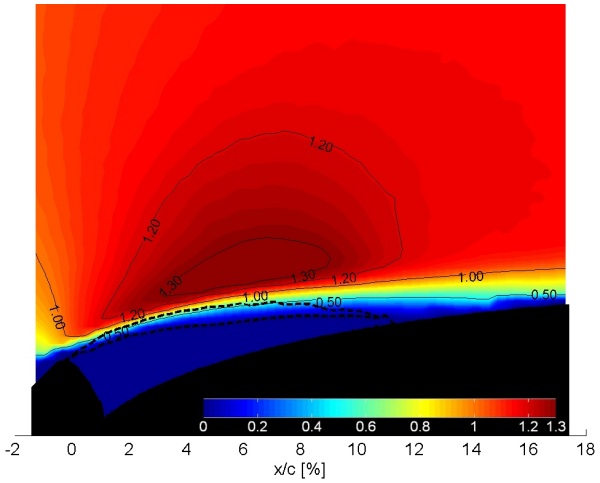

Fig. 16. Mean Streamwise Velocity, $\overline{u}/V_\infty$ [2D Ice Simulation (z/b=0.47), R_e=0.9x10^6, M_∞=0.20, α=0-deg, – – Sep.(Upper) and Stag.(Lower) Streamlines]

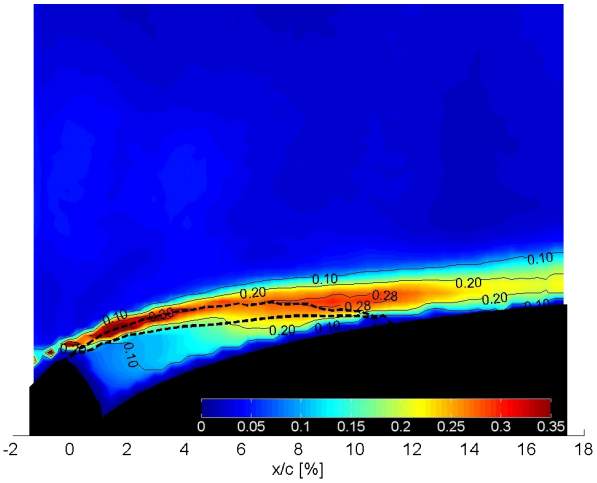

Fig. 19. RMS Streamwise Velocity, u_{RMS}/V_∞ [2D Ice Simulation (z/b=0.47), R_e=0.9x10^6, M_∞=0.20, α=0-deg, – – Sep.(Upper) and Stag.(Lower) Streamlines]

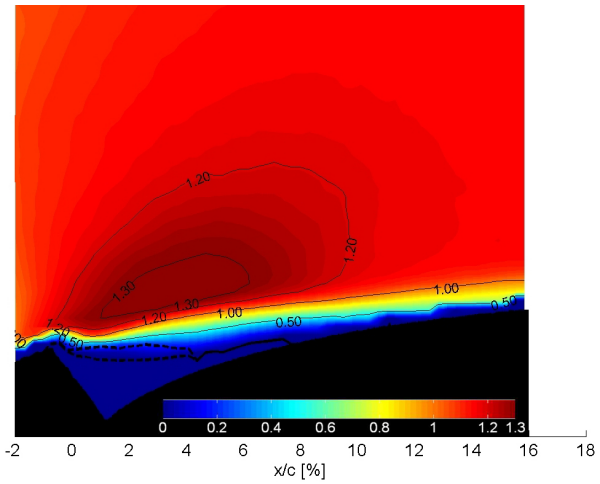

Fig. 17. Mean Streamwise Velocity, $\overline{u}/V_\infty$ [3D Ice Simulation (z/b=0.49), R_e=0.9x10^6, M_∞=0.20, α=0-deg, – – Sep.(Upper) and Stag.(Lower) Streamlines]

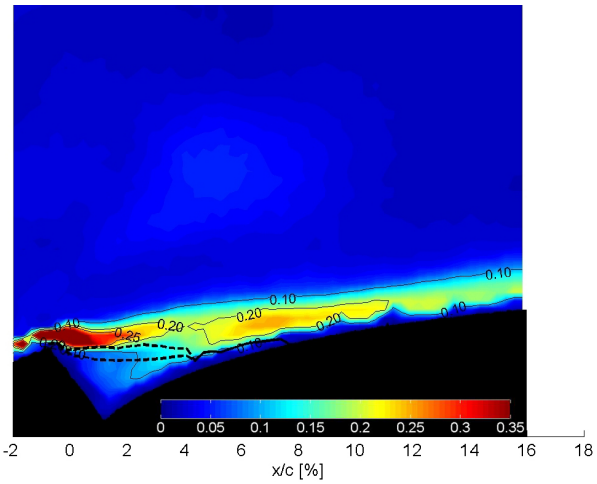

Fig. 20. RMS Streamwise Velocity, u_{RMS}/V_∞ [3D Ice Simulation (z/b=0.49), R_e=0.9x10^6, M_∞=0.20, α=0-deg, – – Sep.(Upper) and Stag.(Lower) Streamlines]

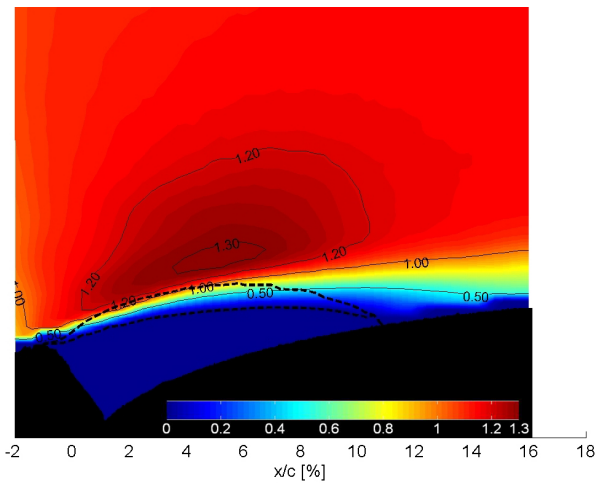

Fig. 18. Mean Streamwise Velocity, $\overline{u}/V_\infty$ [3D Ice Simulation (z/b=0.54), R_e=0.9x10^6, M_∞=0.20, α=0-deg, – – Sep.(Upper) and Stag.(Lower) Streamlines]

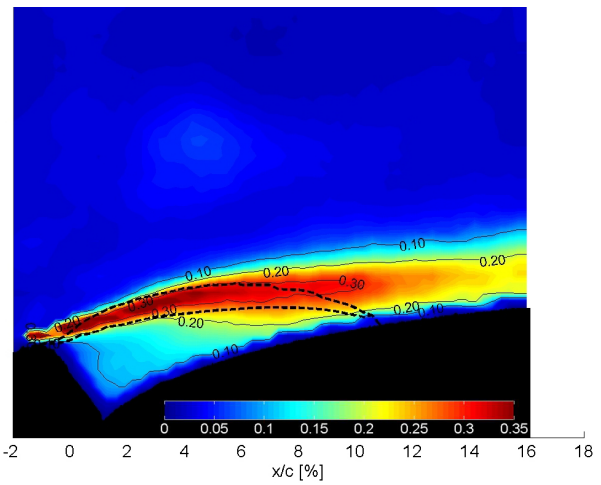

Fig. 21. RMS Streamwise Velocity, u_{RMS}/V_∞ [3D Ice Simulation (z/b=0.54), R_e=0.9x10^6, M_∞=0.20, α=0-deg, – – Sep.(Upper) and Stag.(Lower) Streamlines]

dimensional ice simulation, shown in Fig. 22, is again nearly identical to data for the original two-dimensional ice simulation presented by Jacobs and Bragg.[13] That is, the RMS normal velocity field qualitatively resembles the RMS streamwise velocity field, however, the local peak near mean reattachment is broader in the chordwise direction and shifted downstream and toward the model surface. This indicates that, relative to the magnitude of peak RMS velocities near mean reattachment, fluctuations in the normal direction persist farther downstream before decaying than those in the streamwise direction. The results behind the three-dimensional ice simulation at both spanwise stations likewise follow the same trend.

Chordwise distributions of maximum RMS streamwise and normal velocities are now presented in Figs. 25 and 26. Data for the two-dimensional ice simulation are presented as filled squares (■), for the three-dimensional ice simulation at z/b=0.49 as downward-pointing, open triangles (▽), and for the three-dimensional ice simulation at z/b=0.54 as upward-pointing, open triangles (△). In all cases, RMS velocities are normalized by the freestream velocity and the chordwise coordinate, by the location of mean reattachment. The two-peak chordwise distribution of maximum RMS streamwise velocity is again apparent in Fig. 25 with the larger peak occurring just downstream of flow separation and the smaller, just upstream of mean reattachment, near x/x_{MR}=0.85 for each configuration. Also note beyond approximately x/x_{MR}=1.20, the chordwise distribution of maximum RMS streamwise velocity within the attached, turbulent boundary layer converges for each configuration. It is only in the separated shear layer and just downstream of mean reattachment where the maximum RMS streamwise velocity fluctuations are significantly smaller and larger for the three-dimensional ice simulation at z/b=0.49 and 0.54, respectively, each relative to the two-dimensional ice simulation. Now referring to Fig. 26, note the similar two-peak chordwise distribution of maximum RMS normal velocity. Near mean reattachment, however, these peaks are much broader in the chordwise direction, particularly the three-dimensional ice simulation at z/b=0.49 where the maximum RMS normal velocity is nearly constant at 0.10 between x/x_{MR}=0.50 and 1.50. Each "peak" is also shifted downstream relative to the location of the peak RMS streamwise velocity near mean reattachment with each one centered near x/x_{MR}=1.00. Finally, the chordwise distribution of maximum RMS normal velocity for each configuration does not converge downstream of mean reattachment as in the streamwise direction, rather a

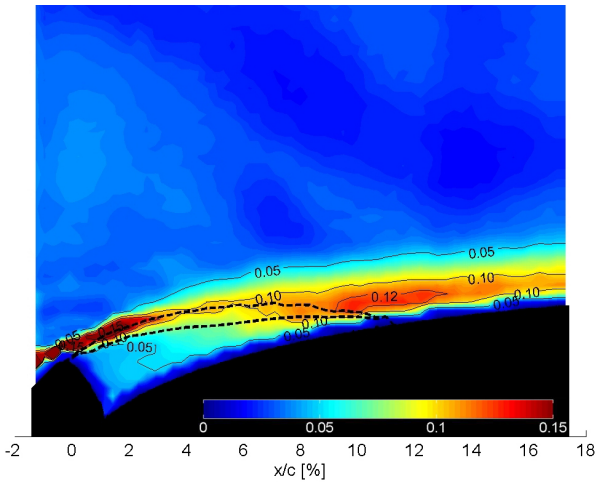

Fig. 22. RMS Normal Velocity, v_{RMS}/V_∞ [2D Ice Simulation (z/b=0.47), R_e=0.9x10^6, M_∞=0.20, α=0-deg, – – Sep.(Upper) and Stag.(Lower) Streamlines]

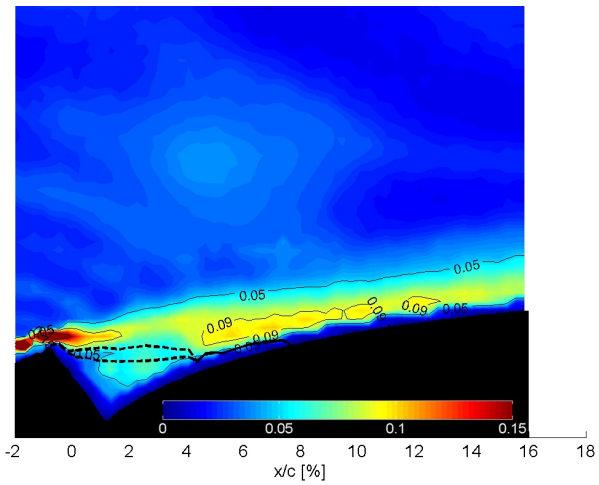

Fig. 23. RMS Normal Velocity, v_{RMS}/V_∞ [3D Ice Simulation (z/b=0.49), R_e=0.9x10^6, M_∞=0.20, α=0-deg, – – Sep.(Upper) and Stag.(Lower) Streamlines]

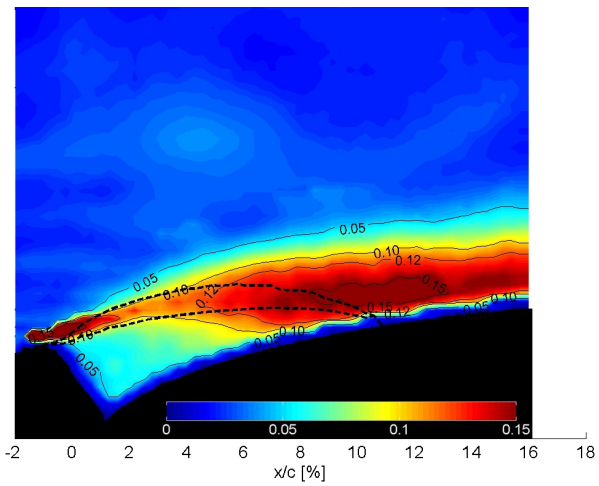

Fig. 24. RMS Normal Velocity, v_{RMS}/V_∞ [3D Ice Simulation (z/b=0.54), R_e=0.9x10^6, M_∞=0.20, α=0-deg, – – Sep.(Upper) and Stag.(Lower) Streamlines]

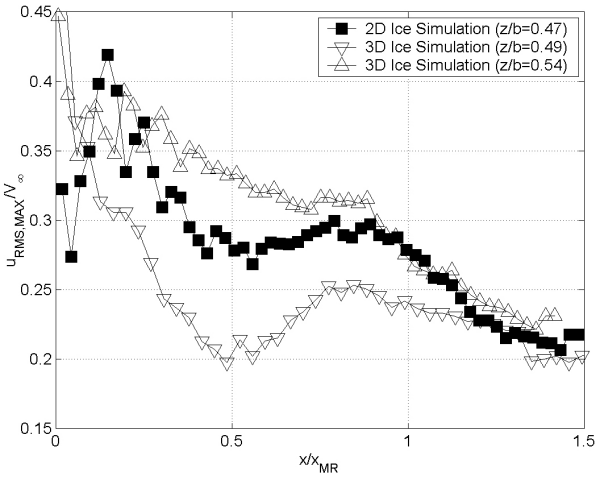

Fig. 25. Maximum RMS Streamwise Velocity, $u_{RMS,MAX}/V_\infty$ [R_e=0.9x10^6, M_∞=0.20, α=0-deg]

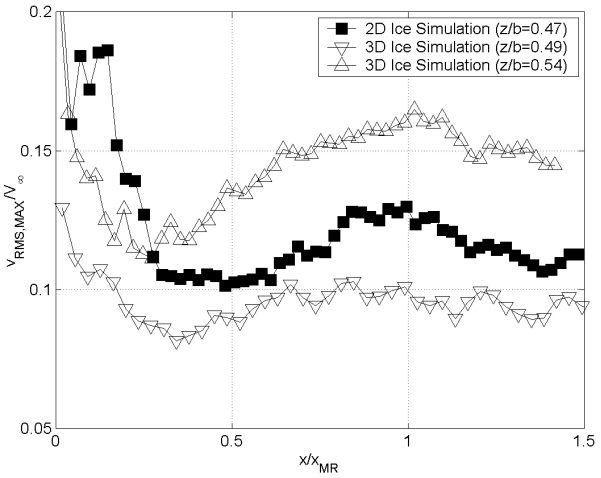

Fig. 26. Maximum RMS Normal Velocity, $v_{RMS,MAX}/V_\infty$ [R_e=0.9x10^6, M_∞=0.20, α=0-deg]

relatively constant offset is observed between each configuration across the chordwise range presented.

Surface-normal profiles of mean streamwise velocity and RMS streamwise and normal velocities are now presented in Figs. 27-29 for the three configurations discussed above. All data are presented at three chordwise locations, upstream of mean reattachment and inside the separation bubble ($\xi/\xi_{MR} = 0.85$), at mean reattachment ($\xi/\xi_{MR} = 1.00$), and downstream of mean reattachment ($\xi/\xi_{MR} = 1.22$), where the variable ξ represents the distance along the airfoil surface from the intersection of the ice simulation and airfoil model ($\xi = 0$, x/c=1.14%) and the estimate of mean reattachment comes from PIV measurements as discussed previously. The symbol legend is the same as described above and all profiles are normalized by the boundary-layer edge-velocity, u_e, to account for the airfoil streamwise pressure gradient and are plotted versus the surface-normal coordinate, η, normalized by the 99% edge-velocity boundary-layer thickness, δ.

First note in Fig. 27 the sign of the skin friction indicated by the slope of the mean streamwise velocity with respect to the surface-normal coordinate at the model surface. The negative slope inside the separation bubble ($\xi/\xi_{MR} = 0.85$) demonstrates the mean streamwise flow near the surface is reversed at this location and the near zero slope at $\xi/\xi_{MR} = 1.00$ implies this location is very near mean reattachment. Finally, downstream of mean reattachment, each configuration displays an attached profile. Next, note how closely the profiles match between configurations when normalized in this manner, particularly the two-dimensional ice simulation and three-dimensional ice simulation at z/b=0.54 which were shown above to be qualitatively very similar in terms of their mean and RMS velocity fields. Likewise, the three-dimensional ice simulation at z/b=0.49 matches the two-dimensional ice simulation quite well above η/δ=0.50 (near the height of the peak RMS streamwise velocity as shown in Fig. 28, and thus the shear-layer center), but below, exhibits less streamwise momentum at each chordwise station presented.

RMS streamwise velocity profiles are presented in Fig. 28 at the same locations as the mean profiles in Fig. 27. The peak RMS streamwise velocity near mean reattachment for the two-dimensional ice simulation was approximately 0.30 normalized by the freestream velocity, or 0.24 normalized by the boundary-layer edge-velocity, virtually identical to the original two-dimensional ice simulation results presented by Jacobs and Bragg.[13] And as with the original, the current two-dimensional ice simulation experienced a sudden decay in peak RMS streamwise velocity downstream of mean reattachment, however, the shift of this peak toward the airfoil surface was not observed as before. The peak RMS streamwise velocity near mean reattachment for the three-dimensional ice simulation at z/b=0.49 was approximately 0.25 and 0.20 normalized by the freestream and boundary-layer edge-velocities, respectively. This peak was more narrow in the surface-normal direction and occurred at a slightly smaller value of η/δ indicating a thinner shear layer positioned closer to the airfoil surface[b] compared to the two-dimensional ice simulation as observed in the RMS streamwise and normal velocity contour plots. Furthermore, this peak decayed downstream of mean reattachment to approximately

[b]The actual height above the airfoil surface is the product of the peak height, $\eta/\delta|_{peak}$ and the boundary-layer thickness, δ, both of which are smaller than in the two-dimensional ice simulation case.

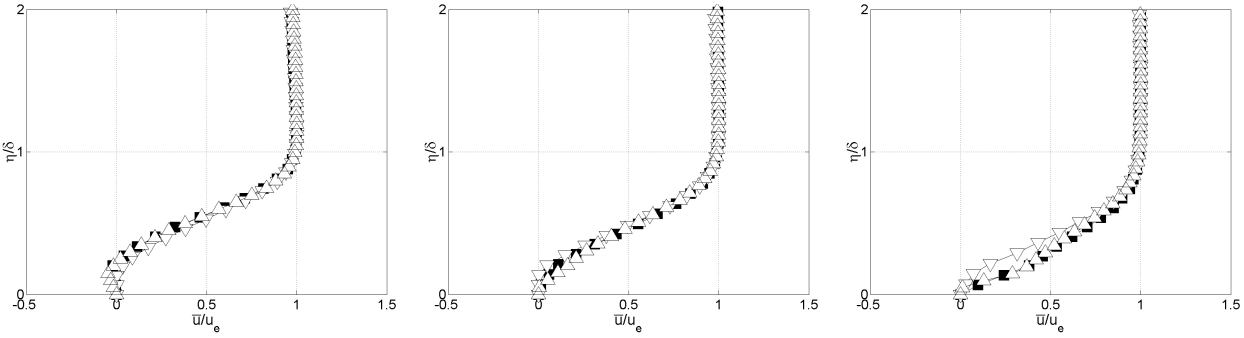

(a) ξ/ξ_{MR}=0.85 (b) ξ/ξ_{MR}=1.00 (c) ξ/ξ_{MR}=1.22

Fig. 27. Mean Streamwise Velocity, $\overline{u}/u_e$ [R_e=0.9x10^6, M_∞=0.20, α=0-deg, ■ 2D Ice Simulation (z/b=0.47), ▽ 3D Ice Simulation (z/b=0.49), △ 3D Ice Simulation (z/b=0.54)]

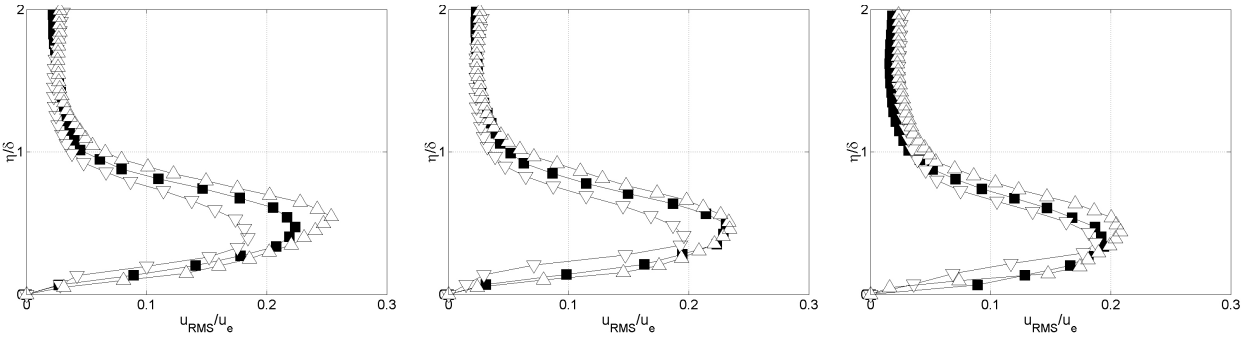

(a) ξ/ξ_{MR}=0.85 (b) ξ/ξ_{MR}=1.00 (c) ξ/ξ_{MR}=1.22

Fig. 28. RMS Streamwise Velocity, u_{RMS}/u_e [R_e=0.9x10^6, M_∞=0.20, α=0-deg, ■ 2D Ice Simulation (z/b=0.47), ▽ 3D Ice Simulation (z/b=0.49), △ 3D Ice Simulation (z/b=0.54)]

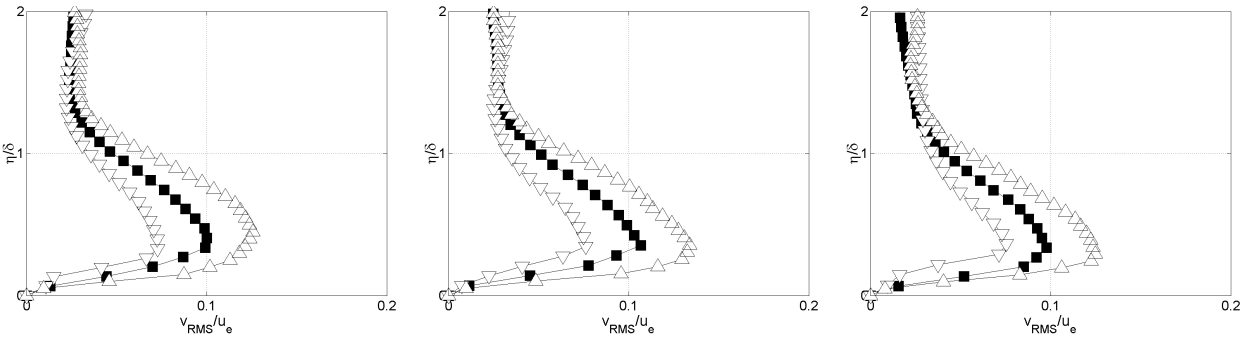

(a) ξ/ξ_{MR}=0.85 (b) ξ/ξ_{MR}=1.00 (c) ξ/ξ_{MR}=1.22

Fig. 29. RMS Normal Velocity, v_{RMS}/u_e [R_e=0.9x10^6, M_∞=0.20, α=0-deg, ■ 2D Ice Simulation (z/b=0.47), ▽ 3D Ice Simulation (z/b=0.49), △ 3D Ice Simulation (z/b=0.54)]

the same value as that of the two-dimensional ice simulation. Finally, the peak RMS streamwise velocity near mean reattachment for the three-dimensional ice simulation at z/b=0.54 was approximately 0.32 and 0.26, again normalized by the freestream and boundary-layer edge-velocities, respectively. In this case, however, the peak was broader in the surface-normal direction and occurred at a larger value of η/δ. As observed from the RMS streamwise and normal velocity contour plots, this implies a thicker shear layer positioned higher above the airfoil surface[c]. And downstream of mean reattachment, the peak RMS streamwise velocity decayed to approximately the same value as for the three-dimensional ice simulation at z/b=0.49 and the two-dimensional ice simulation, as noted from the chordwise distributions of maximum RMS streamwise velocity in Fig. 25, however, the heights of these peaks above the airfoil surface remained staggered as discussed above.

[c]In this case, both the peak height and boundary-layer thickness are larger than in the two-dimensional ice simulation case.

RMS normal velocity profiles are presented in Fig. 29, again at the same locations as the mean and RMS streamwise velocity profiles discussed above. From the contour plots, it was observed that for each configuration, the RMS normal velocity contained a local maximum near mean reattachment as did the RMS streamwise velocity, however, this peak was broader in the chordwise direction and shifted downstream and toward the model surface. This is confirmed by the surface-normal profiles examined here as the peak RMS normal velocities between $\xi/\xi_{MR} = 0.85$ and 1.22 occurred near $\eta/\delta = 0.35$ and were approximately constant at 0.10, 0.08, and 0.13 for the two-dimensional ice simulation and the three-dimensional ice simulation at z/b=0.49 and 0.54, respectively, each normalized by the boundary-layer edge-velocity; with respect to the freestream velocity, these maxima were approximately 0.13, 0.10, and 0.16 as shown in Fig. 26. The peak RMS normal velocities observed for the two-dimensional ice simulation were likewise consistent with those obtained by Jacobs and Bragg[13] for the original two-dimensional ice simulation, however, the height of these peaks remained relatively constant rather than converging toward the airfoil surface as previously observed.

IV. Conclusions

The primary objective of this research was to improve our understanding of the flowfield structure of the separation bubbles formed on a NACA 0012 airfoil with simulated, leading-edge, two- and three-dimensional, glaze-ice accretions. A new 15x15-inch test section wind tunnel was assembled for PIV experiments to investigate these flowfields. An appropriate aspect ratio model and three-dimensional ice simulation were identified which generated sub-scale flowfields consistent with those examined by Gurbacki and Bragg[2] and Gurbacki[3] and hardware was fabricated. Time-averaged pressure distributions and surface oil-flow visualization on this new hardware confirmed that these flowfields were indeed consistent with the full-scale flowfields of interest in terms of mean reattachment behavior with angle-of-attack and spanwise cell structure and spacing.

In general, the time-averaged flowfield with both the two- and three-dimensional ice simulations consisted of a clockwise recirculating, primary separation region enclosed by a shear layer and a smaller, counter-clockwise recirculating, secondary separation region centered at the intersection of the ice simulation and airfoil model, each of which grew in length and height with increasing angle-of-attack. The shear layer was thinner, concave, and contained lower intensity RMS velocity fluctuations, creating a shorter, more circular primary recirculation region behind the three-dimensional ice simulation at a spanwise location near the edge of adjacent spanwise cell structures (z/b=0.49), all relative to the two-dimensional ice simulation flowfield. Toward the center of a spanwise cell (z/b=0.54), however, where surface oil-flow visualization indicated quasi-two-dimensional flow, the three-dimensional ice simulation flowfield was qualitatively very similar to that of the two-dimensional ice simulation, but with a thicker, more convex shear layer containing higher intensity RMS velocity fluctuations. In all cases, PIV images of the seeded flow showed small vortex structures inside the shear layer and larger vortex activity downstream of the separation bubble. And the mean location of shear-layer reattachment, determined from the chordwise distribution of forward flow intermittency and skin friction, was slightly upstream of that observed from surface oil-flow visualization, but within the uncertainty of that estimate and the agreement obtained by Jacobs and Bragg.[13]

Airfoil-surface-normal mean streamwise velocity profiles indicated reverse flow near the model surface inside the separation bubble, zero slope or skin friction at mean reattachment, and attached profiles downstream. RMS streamwise and normal velocity profiles of the two-dimensional ice simulation showed peak values near mean reattachment of approximately 0.24 and 0.10 normalized by the boundary-layer edge-velocity and 0.30 and 0.13 normalized by the freestream velocity, consistent with results obtained on the original two-dimensional ice simulation by Jacobs and Bragg.[13] Compared to these values, peak RMS streamwise and normal velocity fluctuations for the three-dimensional ice simulation were shown to be smaller at z/b=0.49 (edge of spanwise cells) and larger at z/b=0.54 (center of spanwise cell). The shear-layer thickness, or RMS velocity peak width in the surface-normal direction, was also shown to be smaller for the three-dimensional ice simulation at z/b=0.49 and larger at z/b=0.54 and this trend continued beyond mean reattachment, applying to the attached, turbulent boundary-layer thicknesses as well. Finally, in the streamwise direction, the RMS velocity fluctuations of each configuration decayed downstream of mean reattachment to approximately the same value (from different peak values), whereas in the normal directions, these RMS velocity fluctuations persisted much farther downstream, remaining relatively constant across the range of chordwise locations examined.

While this paper has made many comparisons between the two- and three-dimensional ice simulation

flowfields, data analysis is ongoing to better understand the structure of these flowfields and how it is affected by ice simulation three-dimensionality, or in this case, roughness. This analysis includes that of PIV measurements along various spanwise-normalwise planes which is expected to characterize the spanwise flow observed in surface oil-flow visualization and aid in the interpretation of the chordwise PIV results presented here.

V. Acknowledgments

This work was supported by a NASA Graduate Student Researchers Program (GSRP) fellowship in cooperation with the NASA Glenn Research Center. The authors would like to thank NASA Glenn contract monitor Dr. Mark Potapczuk for his guidance throughout this study and Dr. Andy Broeren, University of Illinois Research Scientist, for his assistance during wind tunnel construction, data acquisition, and initial setup of the PIV experiment.

References

[1]Bragg, M. B., Khodadoust, A., and Spring, S. A., "Measurements in a Leading-Edge Separation Bubble due to a Simulated Airfoil Ice Accretion," *AIAA Journal*, Vol. 30, No. 6, 1992, pp. 1462–1467.

[2]Gurbacki, H. M. and Bragg, M. B., "Unsteady Aerodynamic Measurements on an Iced Airfoil," AIAA Paper 2002-0241, 40$^{\text{th}}$ AIAA Aerospace Sciences Meeting & Exhibit, Reno, NV, January 2002.

[3]Gurbacki, H. M., *Ice-Induced Unsteady Flowfield Effects On Airfoil Performance*, Ph.D. thesis, University of Illinois at Urbana-Champaign, Urbana, IL, 2003.

[4]Eaton, J. K. and Johnston, J. P., "Low frequency unsteadiness of a reattaching turbulent shear layer," *Turbulent Shear Flows III*, Third International Symposium on Turbulent Shear Flows, University of California at Davis, September 1981, pp. 162–170.

[5]Driver, D. M., Seegmiller, H. L., and Marvin, J. G., "Time-Dependent Behavior of a Reattaching Shear Layer," *AIAA Journal*, Vol. 25, No. 7, 1987, pp. 914–919.

[6]Kiya, M. and Sasaki, K., "Structure of a turbulent separation bubble," *Journal of Fluid Mechanics*, Vol. 137, 1983, pp. 83–113.

[7]Kiya, M. and Sasaki, K., "Structure of large-scale vortices and unsteady reverse flow in the reattaching zone of a turbulent separation bubble," *Journal of Fluid Mechanics*, Vol. 154, 1985, pp. 463–491.

[8]Cherry, N. J., Hillier, R., and Latour, M. E. M. P., "Unsteady measurements in a separated and reattaching flow," *Journal of Fluid Mechanics*, Vol. 144, 1984, pp. 13–46.

[9]Barkley, D., Gomes, M. G. M., and Henderson, R. D., "Three-Dimensional instability in flow over a backward-facing step," *Journal of Fluid Mechanics*, Vol. 473, 2002, pp. 67–190.

[10]Theofilis, V., Hein, S., and Dallmann, U., "On the origins of unsteadiness and three-dimensionality in a laminar separation bubble," *The Philosophical Transactions of the Royal Society of London, Series A*, Vol. 358, 2000, pp. 3229–3246.

[11]Theofilis, V., "On the spatial structure of global linear instabilities and their experimental identification," *Aerospace Science and Technology*, Vol. 4, 2000, pp. 249–262.

[12]Reehorst, A. L. and Richter, G. P., "New Methods and Materials for Molding and Casting Ice Formations," NASA TM 100126, September 1987.

[13]Jacobs, J. J. and Bragg, M. B., "Particle Image Velocimetry Measurements of the Separation Bubble on an Iced Airfoil," AIAA Paper 2006-3646, 24$^{\text{th}}$ AIAA Applied Aerodynamics Conference, San Francisco, CA, June 2006.

[14]Busch, G., private communication, University of Illinois at Urbana-Champaign, Urbana, IL, July 2005.

[15]Westphal, R. V. and Johnston, J. P., "Effect of Initial Conditions on Turbulent Reattachment Downstream of a Backward-Facing Step," *AIAA Journal*, Vol. 22, No. 12, 1984, pp. 1727–1732.

[16]Bayly, B. J., "Three-Dimensional centrifugal-type instabilities in inviscid two-dimensional flows," *Physics of Fluids*, Vol. 31, 1988, pp. 56–64.

[17]Khodadoust, A., *An Experimental Study Of The Flowfield On A Semispan Rectangular Wing With Simulated Glaze Ice Accretion*, Ph.D. thesis, University of Illinois at Urbana-Champaign, Urbana, IL, 1993.

[18]Kostas, J., Soria, J., and Chong, M. S., "Particle image velocimetry measurements of a backward-facing step flow," *Experiments in Fluids*, Vol. 33, 2002, pp. 838–853.

[19]Hudy, L. M., Naguib, A. M., Humphreys, W. M., and Bartram, S. M., "Particle Image Velocimetry Measurements of a Two/Three-dimensional Separating/Reattaching Boundary Layer Downstream of an Axisymmetric Backward-facing Step," AIAA Paper 2005-0114, 43$^{\text{th}}$ AIAA Aerospace Sciences Meeting & Exhibit, Reno, NV, January 2005.